Journal of Quantitative Spectroscopy & Radiative Transfer 146 (2014) 123–139

Contents lists available at ScienceDirect

Journal of Quantitative Spectroscopy & Radiative Transfer

journal homepage: www.elsevier.com/locate/jqsrt

# Ice cloud single-scattering property models with the full phase matrix at wavelengths from 0.2 to 100 μm

Bryan A. Baum [a,*], Ping Yang [b], Andrew J. Heymsfield [c], Aaron Bansemer [c], Benjamin H. Cole [b], Aronne Merrelli [a], Carl Schmitt [c], Chenxi Wang [d]

[a] SSEC, University of Wisconsin-Madison, 1225 W. Dayton Street, Madison, WI 53706, United States
[b] Texas A&M University, College Station, TX, United States
[c] National Center for Atmospheric Research, Boulder, CO, United States
[d] Earth System Science Interdisciplinary Center, University of Maryland, College Park, MD, United States

ARTICLE INFO

*Article history:*
Received 4 November 2013
Received in revised form
7 February 2014
Accepted 26 February 2014
Available online 11 March 2014

*Keywords:*
Ice clouds
Light scattering
Remote sensing
Radiative transfer

ABSTRACT

Ice cloud bulk scattering models are derived for 445 discrete wavelengths between 0.2 μm and 100 μm. The methodology for deriving these optical models is based on microphysical data from 11 field campaigns using a variety of in situ probes, and incorporates a correction to mitigate the impact of ice particles that shatter at the probe inlets. The models are also based on a new library of ice habit single scattering properties developed for plates, droxtals, hollow and solid columns, hollow and solid bullet rosettes, an aggregate of solid columns, and a small/large aggregate of plates. Three sets of models are developed that assume the use of solid columns only, the aggregate of solid columns only, and a general habit mixture that incorporates all the habits. The consistency of the resulting models is explored. While the general habit mixture provides consistency with in situ microphysical measurements and the closest agreement with polarized reflectivities observed by the POLDER instrument on the PARASOL satellite, the aggregate of severely roughened solid columns provides the closest agreement between solar and infrared optical thicknesses. Finally, spectral results are presented for the shortwave and longwave models.



## 1. Introduction

The inference of cloud macrophysical, microphysical, and optical properties for a given sensor generally requires a comparison of sensor measurements to shortwave-channel reflectivities and/or longwave-channel brightness temperature (BT) simulations for a set of known surface and atmospheric conditions. The measurements may be at high spectral resolution or for a set of narrowband or broadband channels, and may further include polarization. In fact, measurements encompassing all of these characteristics are, or were at one time, provided by passive sensors flying in formation as part of the NASA Earth Observing System A-Train constellation. New instruments are being developed and tested on aircraft or ground-based systems that further extend the range of the measurements.

The physical retrieval approach for inferring ice cloud parameters, e.g., cloud thermodynamic phase and optical thickness, relies on the use of a radiative transfer model to simulate accurately the cloud radiances for a variety of different conditions. The cloud radiance simulations

* Corresponding author. Tel.: +1 608 263 3898; fax: +1 608 262 5974.
*E-mail address:* bryan.baum@ssec.wisc.edu (B.A. Baum).

http://dx.doi.org/10.1016/j.jqsrt.2014.02.029
0022-4073 

require a set of single scattering properties, including the single scattering albedo, extinction coefficient, and the scattering phase function (i.e., the first element of the phase matrix). Additionally, the full phase matrix is required for polarization simulations.

The goal of this study is to document a set of ice cloud bulk models that provide these single scattering properties consistently over a wide wavelength range from the ultraviolet (UV) through the far infrared (Far-IR). The current effort expands upon the derivation of ice cloud bulk single-scattering models at solar wavelengths [1] based on in situ cloud microphysical measurements and single-scattering calculations for different ice habits. While the methodology adopted here is the same as in [1], the models now encompass wavelengths from 0.2 to 100 μm. The single scattering properties are given with respect to the effective diameter ($D_{eff}$), which is proportional to the ratio of the total volume to the total projected area and is defined in Appendix A. Note that the effective diameter is a parameter used in modern climate models to specify the mean size of cloud particles. The use of the effective particle size is now broadly accepted in the radiative transfer community [2]. A key feature of the effective diameter is that the details of the particle size distribution (PSD) are not significant for specifying the bulk radiative properties [3,4].

In turn, the bulk properties are employed in a radiative transfer model to simulate cloud reflectivity and transmission properties for a wide range of conditions (including variations in cloud height, viewing geometry, optical thickness, and effective particle size). Ice cloud optical thickness and effective particle size are inferred by comparing measurements to simulations. The retrieval techniques may use data from solar channels [5–9], infrared (IR) channels [10,11], IR spectra [12,13], polarized reflectivity data [14–17], or combinations thereof [18–20]. While many algorithms are available to infer these ice cloud properties, the question arises as to the consistency of the properties between these different sensors. This question is relevant for studies involving long-term cloud characteristics because there may be gaps in the measurements from any given wavelength region.

Our motivation for continuing the effort to develop bulk scattering property models is that the ice cloud optical thickness inferred from different sensors tends to be inconsistent. For example, Baum et al. [21] noted that the optical thickness values inferred from solar channel data collected during the SUbsonic aircraft Contrail and Clouds Effects Special Study (SUCCESS) field campaign were higher than those obtained from infrared (IR) channels. Comparisons of cirrus optical thickness ($\tau < 3$) between the MODerate-resolution Imaging Spectroradiometer (MODIS) Collection 5 products [7] and active measurements from Cloud-Aerosol Lidar with Orthogonal Polarization (CALIOP, [22,23]) indicate significant differences, with MODIS being higher relative to CALIOP. Zhang et al. [24] investigate differences between MODIS Collection 5 and POLDER optical thickness retrievals, and relate the differences to the assumed scattering properties adopted by each team.

This study summarizes the numerous research advancements that are included in this comprehensive set of ice cloud bulk scattering property models. Results are presented for spectral models at wavelengths from 0.2 to 100 μm that include the full phase matrix. The models include ice particle roughening, which can impact the phase matrix [25]. Models have also been developed for polar-orbiting and geostationary imagers that account for the individual sensor spectral response functions. The goal is to provide models that are built for each sensor using consistent and straightforward methodology.

The single-scattering properties in the spectral models consist of the single-scattering albedo, asymmetry parameter, extinction coefficient, extinction efficiency, total projected particle area, and the full phase matrix, all as functions of the effective diameter. For the various imagers, only the scattering phase function (i.e., $P_{11}$) is provided. This new generation of ice cloud models is anticipated to provide a significant improvement in consistency between sensors over the previous versions. The differences between optical thickness retrievals based on solar and IR techniques will be reduced, as will optical thickness differences between passive and active sensors. Furthermore, the new models are more consistent with polarized reflectivity measurements from sensors such as PARASOL [26].

Section 2 discusses the microphysical data and the library of ice particle single-scattering properties used in the study. Also discussed in this section is the approach adopted to develop both spectral and narrowband bulk single-scattering properties from the microphysical data and ice particle single-scattering property library. Models are developed for three choices of the ice habit: (1) a general habit mixture, (2) solid columns only, and (3) aggregate of solid columns only. Section 3 provides a sense of the consistency of the new ice models. Ice cloud optical thickness is evaluated from comparing solar and infrared (IR) techniques, and also comparing to historical MODIS Collection 5 ice cloud optical thickness. Results from the new models across the spectrum from the UV to the Far-IR are presented in Section 4, and Section 5 concludes.

## 2. Data and models

### 2.1. Microphysical data

The microphysical data provide information on particle size distributions (PSDs) as well as the ice water content (IWC) and the median mass diameter ($D_{mm}$, i.e., the diameter at which half the mass in the PSD is in smaller particles and half in larger particles). The data are based on a series of ice cloud field campaigns listed in Table 1. A detailed summary of these data is provided in [27] and Table 1 provides information on the location of the 11 field campaigns and the sensors used for measuring the particle size spectra. The field campaigns were held in a variety of midlatitude and tropical locations, including sites from both the hemispheres. The fitting coefficients for the gamma distribution are provided for each individual particle size distribution (PSD), as well as the maximum diameter that should be used for the spectra. The maximum diameter is the size of the largest observed particle, which is partially dependent on the sensor used to derive the specific dataset.

**Table 1**
More than 14,000 PSDs are used in this study after filtering the total sample set such that the cloud temperature $T \leq -40$ °C. The data are revised to reflect better consistency between probes and to account for refinement of processing procedures. The field campaigns include the Atmospheric Radiation Measurement program Intensive Observation Period (ARM-IOP); Tropical Rainfall Measuring Mission (TRMM); Cirrus Regional Study of Tropical Anvils and Cirrus Layers Florida Area Cirrus Experiment (CRYSTAL-FACE); Aura Validation Experiment (pre-AVE, 2004); Midlatitude Cirrus Experiment (MidCiX, 2004); Stratospheric-Climate links with emphasis On the Upper Troposphere and lower stratosphere (SCOUT); Aerosol and Chemical Transport in tropIcal conVEction (ACTIVE); Mixed Phase Arctic Cloud Experiment (MPACE); and Tropical Clouds, Convection, Chemistry, and Climate (TC4). The different probe types include the 2-Dimensional Cloud probe (2-DC), the 2-Dimensional Precipitation probe (2-DP), the Cloud Particle Imager (CPI), the Video Ice Particle Sampler (VIPS), the Precipitation Imaging Probe (PIP), the Cloud, Aerosol, and Precipitation Spectrometer (CAPS), and the Forward Scattering Spectrometer Probe (FSSP). Ice water content measurements are from the Counterflow Virtual Impactor (CVI), the Closed-path tunable diode Laser Hygrometer (CLH), or the Harvard University Lyman-α total water photofragment-fluorescence hygrometer (HT), and m-D refers to when a mass dimensional relationship was used to estimate the ice water content.

| Field campaign | Year | Location | Number of 5-s averaged PSDs $T_{cld} \leq -40$ °C | Probes | IWC |
|---|---|---|---|---|---|
| ARM IOP | 2000 | Oklahoma, USA | 1420 | 2D-C, 2D-P, CPI | CVI |
| TRMM KWAJEX | 1999 | Kwajalein, Marshall Islands | 201 | 2D-C, HVPS, CPI | m-D |
| CRYSTAL-FACE (from WB-57) | 2002 | Caribbean | 221 | CAPS, VIPS | CLH |
| SCOUT | 2005 | Darwin, Australia | 358 | FSSP, 2D-C | m-D |
| ACTIVE-Monsoons | 2005 | Darwin, Australia | 4268 | CAPS | m-D |
| ACTIVE-Squall Lines | 2005 | Darwin, Australia | 740 | CAPS | m-D |
| ACTIVE-Hector | 2005 | Darwin, Australia | 2583 | CAPS | m-D |
| MidCiX | 2004 | Houston, TX USA | 2968 | CAPS, VIPS | CLH |
| Pre-AVE | 2004 | Houston, TX, USA | 99 | VIPS | HT |
| MPACE | 2004 | Prudhoe Bay, Alaska | 671 | 2D-C, CPI | m-D |
| TC-4 | 2007 | Costa Rica | 877 | CAPS, PIP | CVI |

The sets of available PSDs listed in the table are filtered such that $T_{cld} \leq -40$ °C to ensure that we are working with ice cloud measurements. Even with this conservative temperature filter, more than 14,000 PSDs remain and are used in this study. For perspective, these PSD measurements are taken from over 70,000 km of flight tracks. These data encompass both convective outflow and stratiform ice clouds, with IWC values spanning six orders of magnitude from $10^{-6}$ to $10^{0}$ g m$^{-3}$. The IWC is obtained from direct measurements or by applying a mass–dimensional relationship [27]. The approach of Schmitt and Heymsfield [28] is used for high altitude cases.

For ice clouds that contain large particles, it has been shown that small particle concentration measurements are influenced by shattering at the inlet of the 2D-C (and similar) probes [29–31]. Since the data used here are filtered for very cold clouds ($T_{cld} \leq -40$ °C), particle shattering should not generally be a large problem due the lack of very large particles except in cases of deep convection. Where shattering is a problem, it is most evident in the total concentration measurement since total concentration is usually dominated by the smallest particles. However, the effect of shattering is diminished when the PSD is weighted to larger particle sizes, such as in computing IWC, $D_{mm}$, or any other higher moment and when dividing two moments of similar magnitudes such as in deriving the effective radius [31]. The data used in this study were reprocessed to mitigate the shattering issue for all the 2D probe data as described by Field et al. [31]. Also, we note that small particle data were obtained by balloon borne replicators for ARM and small particle probes were used for SCOUT where only small particles were observed. For the other field programs, small particles had little contribution [32].

The microphysical data for all PSDs used in this study are available for electronic download through the link provided in Table 2.

### 2.2. Ice particle single scattering properties

The single-scattering properties are provided in a database [33] for nine different ice particle habits: droxtals, plates, solid and hollow columns, solid and hollow bullet rosettes, an aggregate of solid columns, and both a small and large aggregate of plates. The ice habit single-scattering properties are based on a combination of the Amsterdam Discrete Dipole Approximation (ADDA), the T-matrix method, and the improved geometric-optics method (IGOM) [33]. The single-scattering properties are provided for each habit at 189 discrete sizes between 2 and 10,000 μm and for 445 discrete wavelengths ranging from 0.2 to 100 μm. The 445 discrete wavelengths are defined as follows. For this study, the properties are interpolated at a 0.01–μm resolution at wavelengths between 0.2 and 3 μm (280 discrete wavelengths) and at a 0.1-μm resolution between 3 and 15 μm (120 discrete wavelengths). The remaining 45 discrete wavelengths are defined between 16 and 100 μm at the inflection points of the imaginary index of refraction (as shown in [33]). The single scattering properties can be interpolated if properties are desired at different wavelengths.

A summary of the primary improvements in the accuracy of the single-scattering properties is as follows:

- The accuracy of the extinction and absorption efficiencies at moderate to large size parameters is improved due to the use of an empirical approach to include the edge and the above/below-edge effects on ice particles [33].
- Recent studies discuss the impact of surface roughening on ice particle properties inferred from measurements [34,35]. In this study, three surface roughness conditions are considered: smooth, moderately roughened, and severely roughened particles [36].
- A new analytical treatment of forward scattering in the IGOM renders obsolete the delta transmission energy

**Table 2**
Links to the microphysical data, spectral models, and narrowband models.

| Data or model | Link | Comments |
|---|---|---|
| Microphysical data | http://www.ssec.wisc.edu/ice_models/microphysical_data.html | For field campaigns in Table 1 |
| Spectral models from 0.2 to 100 μm | http://www.ssec.wisc.edu/ice_models/polarization.html | At 445 individual wavelengths; NetCDF |
| Narrowband models for various sensors | http://www.ssec.wisc.edu/ice_models/imager.html | For sensors in Table 3; NetCDF |

**Table 3**
Satellite sensors for which narrowband models are available. The models are built with the general habit mixture and assume that the particles are severely roughened.

| Satellite imager | Platforms | Name and notes |
|---|---|---|
| AVHRR | NOAA 5–19; MetOP A/B | Advanced Very High Resolution Radiometer |
| MODIS | Terra/Aqua | Moderate Resolution Imaging Spectroradiometer |
| MISR | Terra | Multiangle Imaging SpectroRadiometer |
| AATSR | | Advanced Along-Track Scanning Radiometer |
| IIR | CALIPSO | Imaging Infrared Radiometer |
| VIIRS | Suomi-NPP | Visible Infrared Imaging Radiometer Suite |
| ATSR | Imager 1–2 | Along Track Scanning Radiometer |
| SEVIRI | METEOSAT Second Generation | Spinning Enhanced Visible and InfraRed Imager |
| GOES | GOES–8 through GOES–13 | Geostationary Operational Environmental Satellite |
| MTSAT | 1–2 | Multifunctional Transport Satellites |
| GOES ABI | GOES-R | Advanced Baseline Imager; New series of GOES; set to launch in 2015 |

term [37]. This term was an artifact of the numerical treatment of forward scattering in earlier studies [38].
- The extinction efficiency does not have a constant value of 2 in the current version of IGOM and now considers the variation of the extinction efficiency as a function of size parameter [33].
- The single-scattering calculations are based on an updated compilation of the real and imaginary parts of the refractive index for ice [39].
- The phase matrix elements for randomly oriented ice particles are provided in the database.

### 2.3. Ice particle general habit mixture

A general habit mixture (GHM) scheme that incorporates all the nine available ice particle habits [1,26] is adopted here with minor changes to the percentages of habits in the smallest size bins. The percentage of droxtals was decreased slightly in favor of increasing plates, columns, and rosettes. The maximum diameter permitted for plates, solid columns, and hollow columns is 500 μm. The hollow/solid bullet rosettes and the three aggregate habits are used for the largest particles in a size distribution. The fraction of a given habit changes linearly with size so as to minimize abrupt changes in average single-scattering properties across size boundaries. Each PSD has an upper limit for the maximum size particle used in its derivation, so the largest size particles may not be used for many of the extremely cold clouds where only smaller sizes exist.

### 2.4. Spectral models

Ice cloud bulk scattering models are developed for a given wavelength by integrating over both particle size and habit distributions for a given wavelength as shown in Appendix A. This process results in a set of over 14,000 calculations of the single scattering properties for every wavelength provided in the single-scattering property database. While this might seem abundant, there are retrieval approaches that require estimates of the variability of the individual single scattering properties. Such variability can be used in optimal estimation applications or described in terms of Jacobians (i.e., partial derivatives) for data assimilation studies.

From this full set of calculations, the single scattering properties are averaged in narrow intervals about selected $D_{eff}$ values to make a limited set of models that is more manageable for radiative transfer calculations. The single-scattering albedo, asymmetry parameter, extinction coefficient, extinction efficiency, total projected particle area, and phase matrix are provided as functions of the effective diameter that ranges from 10 to 120 μm in increments of 5 μm for a total of 23 individual $D_{eff}$ values.

The spectral models of bulk ice cloud single-scattering properties discussed in this and following sections are available for electronic download through the link provided in Table 2.

### 2.5. Imager (narrowband) models

Narrowband models are calculated by integrating the spectral models over a wavelength interval encompassed by a given imager spectral response function. The integration details are provided in Appendix A. The narrowband models of bulk ice cloud single-scattering properties are available for electronic download through the link provided in Table 2. Table 3 lists the imager models currently available.

## 3. Evaluation of model consistency

One of our goals is to work towards a single-scattering property model that improves the consistency in the remote sensing of ice cloud properties between different sensors. This is currently an issue, as shown in a study that compared ice cloud optical thickness retrievals between POLDER and MODIS Collection 5 products [24] that revealed significant differences. The differences were attributed to the assumed single scattering properties. The MODIS Collection 5 models assume smooth ice particles and the POLDER model employs the Inhomogeneous Hexagonal Monocrystal (IHM) model [17]. The IHM model introduces inhomogeneities within the particle, resulting in a featureless scattering phase function (i.e., no halos or other maxima other than the forward scattering peak) as well as a lower asymmetry parameter than a smooth particle model.

One way of evaluating the consistency of the ice models is by imposing a set of constraints. In this section, three questions are discussed in further detail: (1) are the model microphysical properties (IWC and $D_{mm}$) derived from the simulated ice habits similar to those from the in situ measurements, (2) do simulated polarized reflectivities based on the ice models compare reasonably well to those from PARASOL measurements of ice clouds over ocean, and (3) are the optical thickness values consistent when inferred from solar and IR wavelengths?

Models based solely on solid columns are used to derive CERES cloud products [9]. Recently, aggregates of solid columns were adopted for deriving MODIS Collection 6 cloud products rather than a habit mixture as adopted for Collection 5. There are evidently many points of view to consider when choosing a habit or habit mixture for the ensuing global operational data reduction. The habit mixture captures more of the complexity of natural ice clouds than adopting a single habit. However, what really matters is whether the habit choice is sufficient for a given application. Some constraints to consider when choosing a habit model are discussed in more detail below.

Results are presented in this and following sections based on the GHM and two individual habits: aggregates of solid columns (ASC) and solid columns (SC). To be clear, the ASC and SC models employed in the following analyses are not the same models adopted by the CERES or MODIS teams, but are our own models based on these individual habits.

### 3.1. Comparison of computed to measured microphysical properties

The bulk properties are computed for each PSD by integrating the individual habit properties over the size range for an assumed habit profile [1]. Details are provided

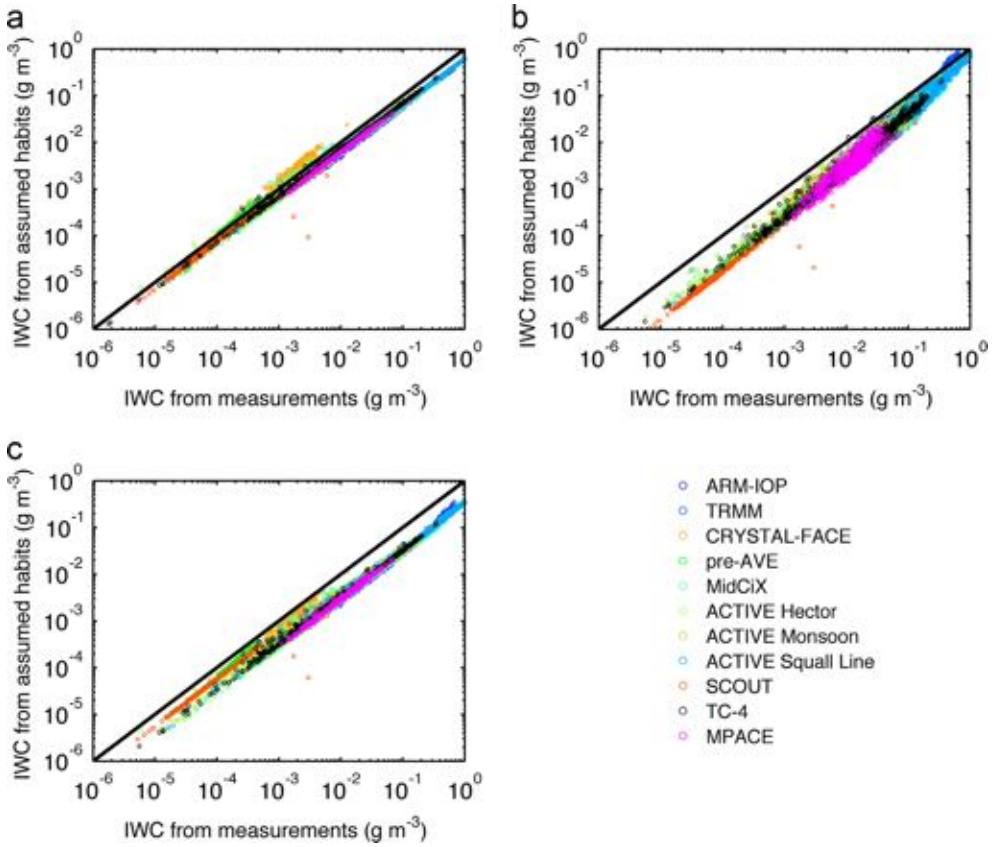


**Fig. 1.** Comparison of calculated to measured ice water content (IWC) for each of the particle size distributions listed in Table 1, assuming the use of (a) solid columns only, (b) aggregate of solid columns only, and (c) a general habit mixture.

in Appendix A to show how the microphysical properties of IWC and $D_{mm}$ are estimated from the ice habits and PSDs.

Fig. 1 shows a comparison of the measured to calculated IWC values for the individual PSDs from the various field campaigns listed in Table 1. Since field campaigns provide invaluable data for validating satellite products, the goal is for IWC to compare reasonably well to those values provided from the in situ measurements. The comparisons from the SC provide the closest match (Fig. 1a), while the ASC results have a higher bias at low IWC values than at higher IWC values. The ASC was intended for use as a large ice particle; for very small particles diameters, the columns are so small that the particle has a lower volume than some of the other habits such as the droxtal and column, leading to lower values of the IWC. The GHM compares reasonably well with the IWC values over much of the range.

Fig. 2 shows the comparison of $D_{mm}$ between the calculated values and those derived from the in situ measurements. Again, the SC results (Fig. 2a) provide the closest comparison with the in situ measurements. However, the adoption of the ASC results in a general overestimation of $D_{mm}$ for the reason discussed previously; at small sizes, the columns in the aggregate are very small, leading to low volumes and hence mass per particle. The GHM results compare favorably with the in situ measurements at $D_{mm}$ values lower than about 400 μm, but overestimate the $D_{mm}$ at higher values.

### 3.2. Comparison of model to PARASOL polarized reflectivities

The issue of particle roughening discussed earlier raises a number of questions as it impacts the various phase matrix components [25]. Since halos are often observed, one can make the argument that there are times for which at least some of the ice particles in a given distribution are smooth and fairly free of internal inhomogeneities. If roughening is to be used as a surrogate for all the internal inhomogeneities, incomplete facets, and surface characteristics for a distribution of ice particles, how much roughening is appropriate for use with global satellite retrievals?

Polarized reflectivity measurements provide a unique perspective to the issue of particle roughening. In a study that compared model-simulated polarized reflectivities to PARASOL measurements over ocean [26], it was shown that in addition to the general habit mixture, there are several individual habits that can match the PARASOL measurements closely, e.g., the hollow 3D bullet rosette, the hollow column, and the small aggregate of plates (cf. Fig. 6 of that study). The use of the general habit mixture and the assumption of severe particle roughening leads to the closest comparison with measured polarized reflectivities over a range of side to back-scattering angles. The following results are an extension of this earlier work, and assume the presence of severe roughening, thereby forgoing further discussion of smooth or moderately roughened particles.

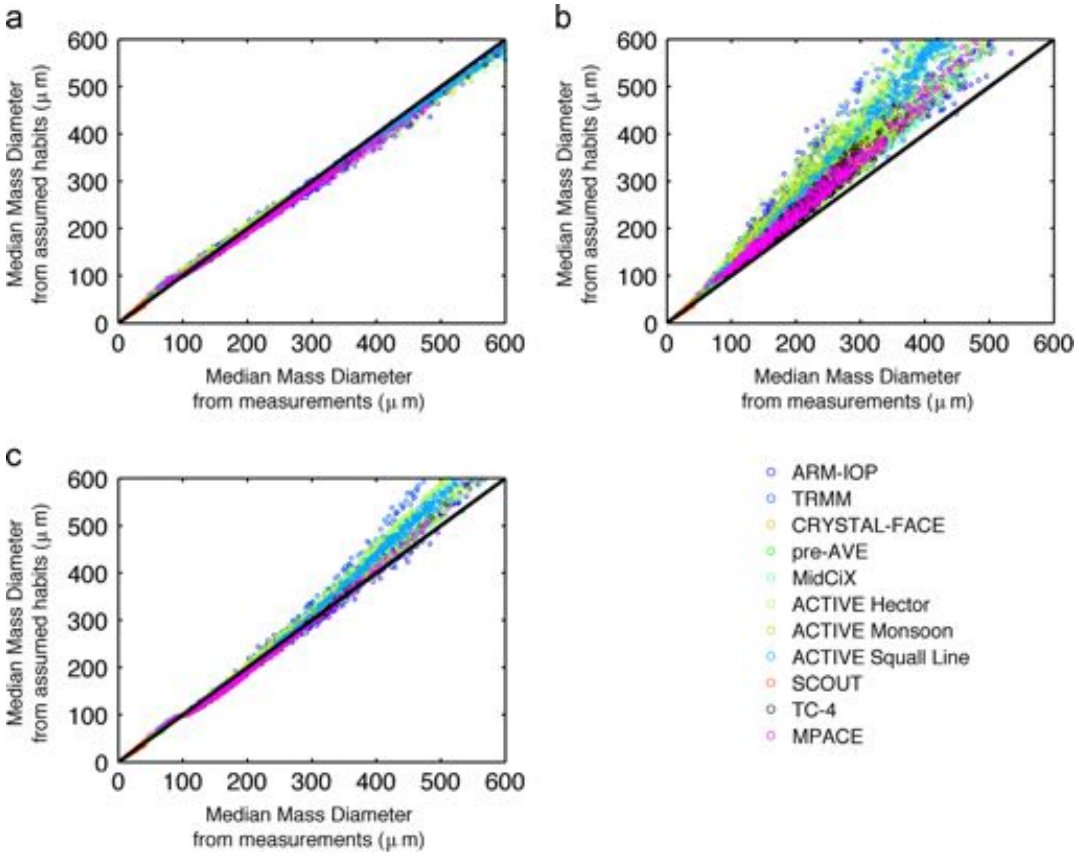


**Fig. 2.** Comparison of calculated to measured median mass diameters ($D_{mm}$) for each of the particle size distributions listed in Table 1, assuming the use of (a) solid columns only, (b) aggregate of solid columns only, and (c) a general habit mixture.

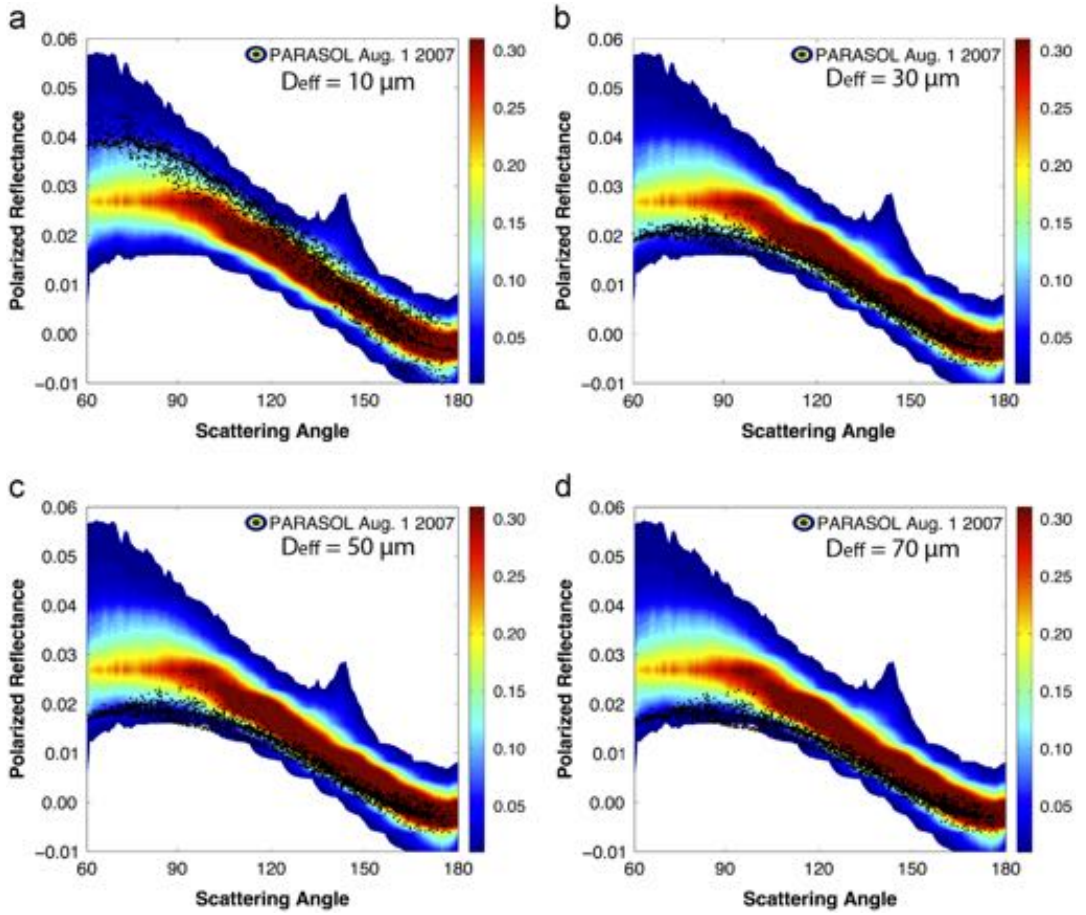


**Fig. 3.** A comparison of normalized polarized reflectivities obtained from one day of PARASOL data over ocean (1 August, 2007) in the color contours to calculations (black dots) based upon an ice cloud model built assuming a single habit of solid columns (SC) for effective diameters ($D_{eff}$) of (a) 10 μm, (b) 30 μm, (c) 50 μm, and (d) 70 μm. The PARASOL color contours represent the frequency of occurrence for a given reflectivity, with the red color denoting the region having the highest occurrences for the day of data. The variability in the calculated polarized reflectivities occurs because a large range of viewing angle combinations (solar zenith, viewing zenith, and relative azimuth) was used, and many combinations of these angles can result in a similar scattering angle. Note that the black dots do not tend to match the PARASOL polarized reflectivities very closely over the range of scattering angles.

The simulations based on the SC model are compared to a day of PARASOL polarized reflectivities as shown in Fig. 3. The four panels correspond to the use of different SC model $D_{eff}$ values of 10 μm, 30 μm, 50 μm, and 70 μm. In this figure, the color contours represent the frequency of occurrence of PARASOL polarized radiances for ice clouds from August 1, 2007, over ocean from 60°N to 60°S. The red contour represents a region of high occurrence for the measured radiances and the blue contour represents a region of very low occurrence. The figure also shows a set of black dots; each black dot represents a model calculation for a given set of viewing angles (solar zenith, viewing zenith, and relative azimuth) provided in the PARASOL data, with the further assumption that there is an ice cloud with an optical thickness of 5, i.e., an ice cloud with a high enough optical thickness so that the polarized reflectivity is saturated. The polarization signal decreases because of multiple scattering as optical thickness increases. Note that the simulations do not match the PARASOL data very closely for any of the $D_{eff}$ values, especially at side scattering angles.

Fig. 4 shows similar results but based on the ASC model. At no $D_{eff}$ value do the simulations match well with the measurements over the range of scattering angles. For all $D_{eff}$ values, the polarized reflectivities calculated from the ASC model tend to be lower than the measurements except near backscattering angles. While not shown, the comparison between simulated and measured polarized reflectivities is not favorable based on models that assume an individual habit.

Cole et al. [26] demonstrated that use of the GHM for a range of $D_{eff}$ values resulted in consistent comparisons with measured reflectivities for a single day of global data over ocean (see Fig. 5 of [26]). A question that was not addressed is whether these same models will result in consistent comparisons with PARASOL over time. Fig. 5 shows similar comparisons for one day in each of the four different seasons, based on the GHM for $D_{eff}$ =60 μm.

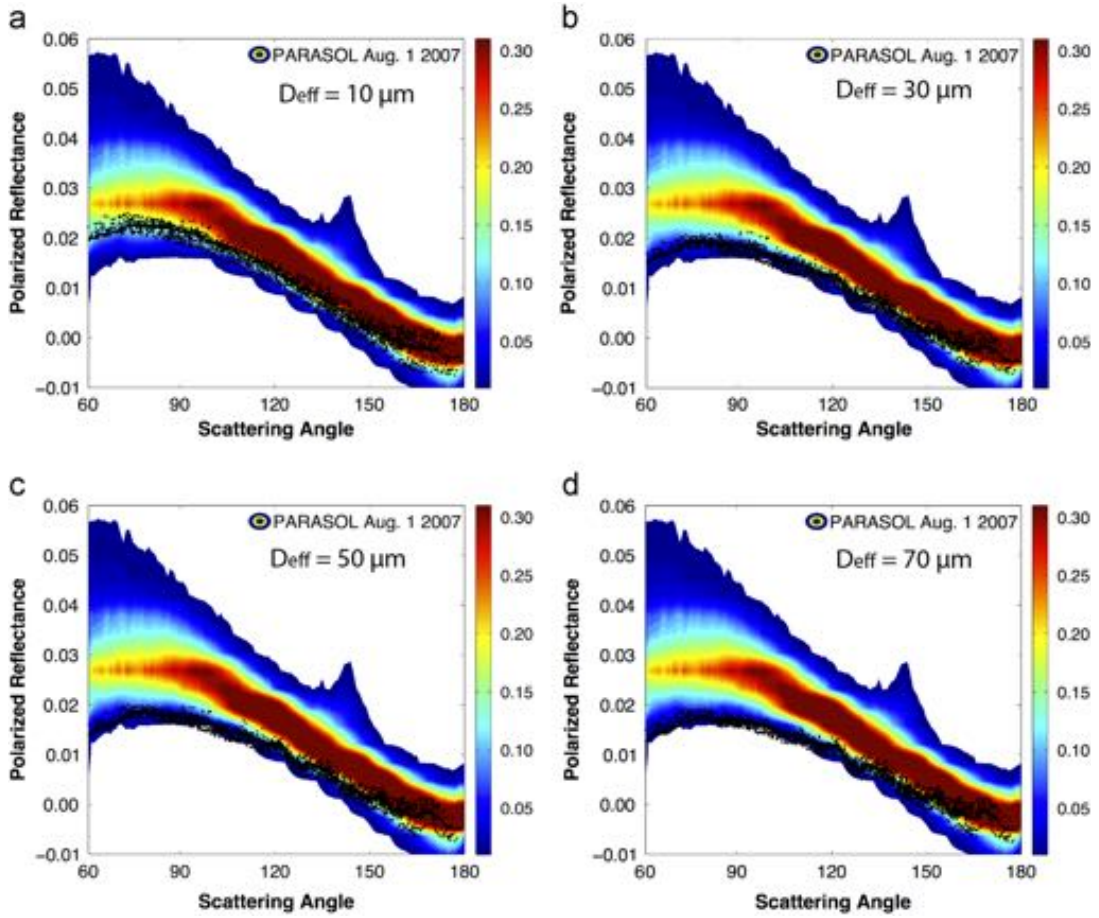


**Fig. 4.** Same as Fig. 3 but assuming the use of only the aggregate of solid columns. Results are shown for (a) $D_{eff}$=10 μm, (b) $D_{eff}$=30 μm, (c) $D_{eff}$=50 μm, and (d) $D_{eff}$=70 μm. Note that the simulations (black dots) again do not tend to match the PARASOL polarized reflectivities very closely, especially at side scattering angles.

The simulations generally match well with PARASOL measurements over the range of scattering angles for each of these days. It would be interesting to focus more specifically on optically thin cirrus in future comparisons, since the assumption made in the simulations is that the ice clouds are optically thick from a polarization perspective.

However, the general habit mixture compares closely to the measured IWC and $D_{mm}$ in the in situ measurements as shown in the previous section. The closest match between simulations and measurements occurred for particles that were severely roughened with $\sigma$=0.5.

In a new study, Cole et al. [40] perform multiple retrievals for each PARASOL pixel and test individual habit models as well as the habit mixture for a range of roughening values. Surprisingly, the aggregate of solid columns is determined to be the preferred habit in the tropics, although with a lower roughening value of $\sigma$=0.2, while more pristine particles are preferred at higher latitudes. It may be that with ice clouds formed from deep convection, the particles near cloud top have more irregularities (i.e., roughening) than ice particles that form in synoptic cirrus at higher latitudes that have much lower updraft velocities. Our results suggest that none of the nine individual habit models can match adequately the polarized reflectivities observed in global data.

The information in polarized reflectivity measurements is primarily useful for stratiform cirrus rather than deep convective clouds. The reason is that the polarization signal decreases with multiple scattering, so the interpretation of the data most likely corresponds to the upper portions of the ice clouds. Clearly more research needs to be done in this area to resolve some of these questions.

### 3.3. Comparison of solar to IR optical thicknesses

Another way to assess the consistency of cirrus optical thickness ($\tau$) retrievals is to compare results obtained separately using solar and IR measurements. A case study is provided to illustrate the solar and IR $\tau$ retrievals for a MODIS–Aqua granule recorded over the Bay of Bengal at 0745 UTC on 2 August, 2010 as shown in Fig. 6.

For this analysis, two different fast models are employed to infer optical thickness. The solar-based method [41] infers optical thickness $\tau$ by minimizing the differences between model simulations and observations

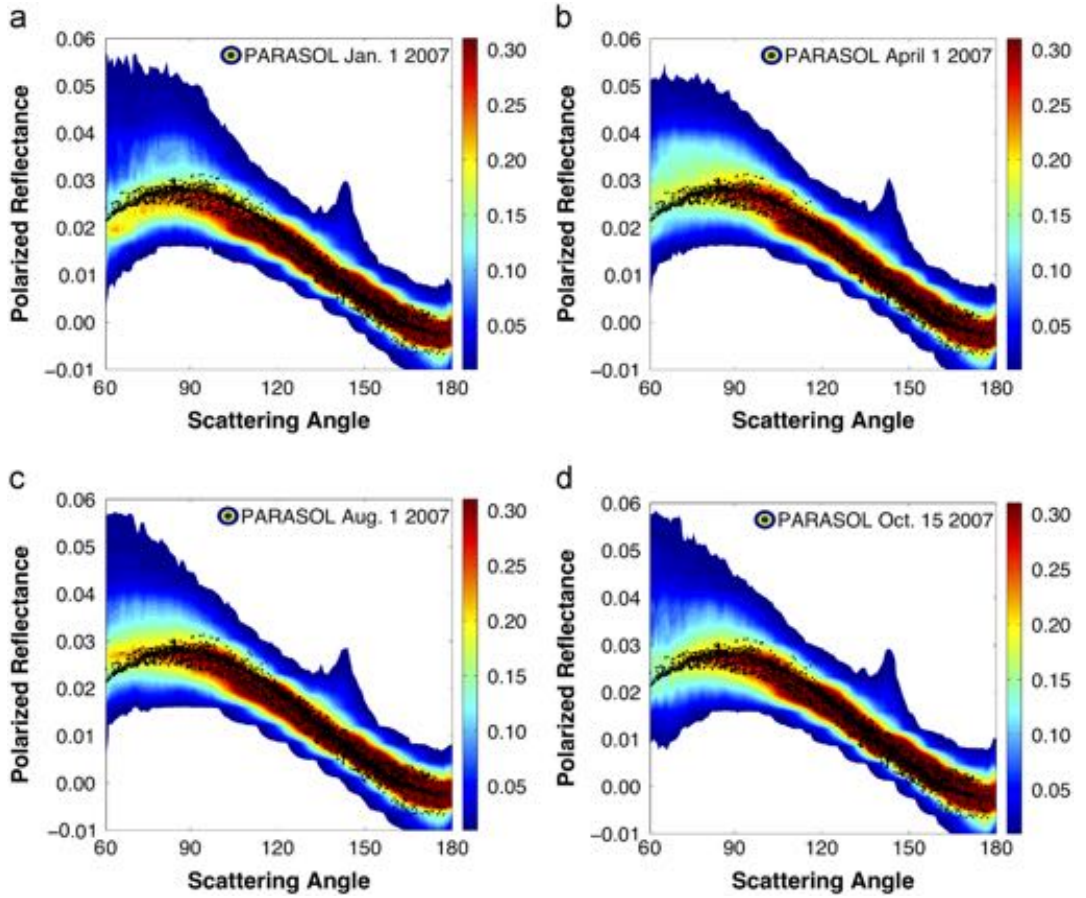


**Fig. 5.** Comparison of PARASOL measurements of ice cloud polarized reflectivities over ocean (in the color contours) with simulations (black dots) based on ice model bulk scattering properties developed using a general habit mixture (GHM) assuming $D_{eff}$=60 μm for one day in four seasons: (a) 1 January, 2007, (b) 1 April, 2007, (c) 1 August, 2007, and 15 October, 2007. Note that the black dots mimic the PARASOL polarized reflectivities consistently for all four days.

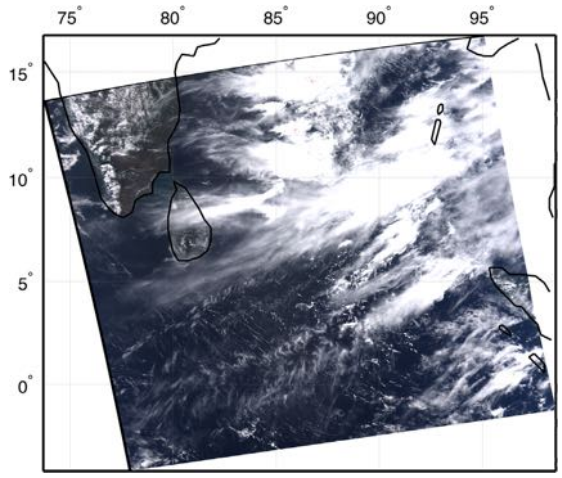


**Fig. 6.** Aqua/MODIS scene from 2 August, 2010, recorded over the Bay of Bengal at 0745 UTC.

at 0.86 and 2.13 μm (MODIS bands 2 and 7, respectively). The IR-based method [42] computes optical thickness by minimizing the difference between measured and computed radiances in the 8.5, 11, and 12 μm bands (MODIS bands 29, 31, and 32 respectively).

A brief description of how the models are used is as follows. The IR fast model simulates top-of-atmosphere brightness temperatures (BTs) for three MODIS channels by using different $\tau$-$D_{eff}$ pairs. The retrieval begins from a set of model simulations at $m$ $\tau$ values and $n$ $D_{eff}$ values. A search is made through each of the $m \times n$ $\tau$-$D_{eff}$ pairs to determine which pair has the minimum model-observation differences (or cost function). Based on this initial $\tau$-$D_{eff}$ pair, the program refines the $\tau$-$D_{eff}$ search by searching approximately 100 different $\tau$-$D_{eff}$ pairs within a small interval, and the $\tau$-$D_{eff}$ pair with the minimum cost function is considered to be the final result. The solar model employs a similar methodology but is based on channel reflectivities.

Fig. 7 shows comparisons of the IR-based optical thickness retrievals for the three different habit models. The comparisons are shown as histograms of frequency of occurrence for optical thickness values on a log 10 scale, with red indicating the highest frequencies of occurrence. Histograms are shown based on comparisons between (a) the GHM and the ASC, (b) the solid column and the ASC

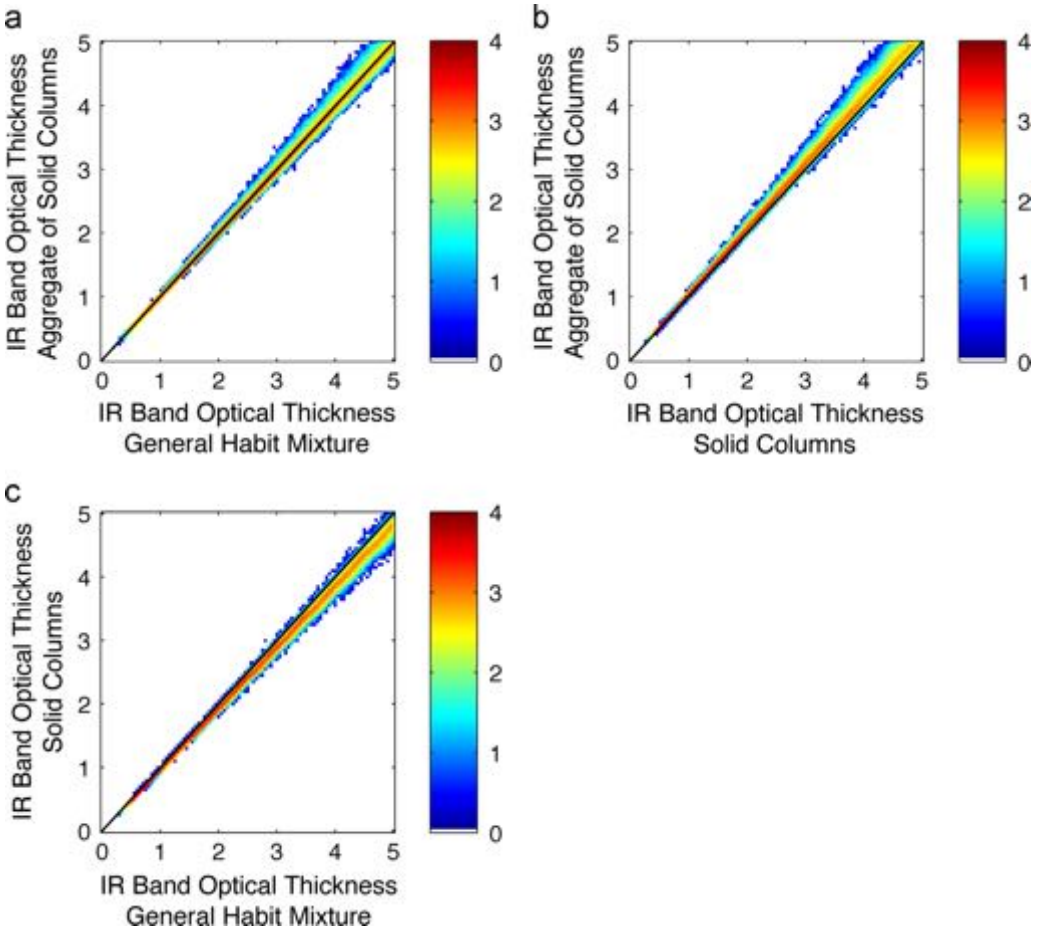


**Fig. 7.** Comparison of ice cloud optical thicknesses based on a fast model that minimizes the differences between measured and computed radiances in the 8.5, 11, and 12 μm bands (MODIS bands 29, 31, and 32 respectively). The IR optical thicknesses are based on different ice habit models for the MODIS granule shown in Fig. 3. Histograms are shown based on results (a) for the general habit mixture and the aggregate of solid columns, (b) the solid column and the aggregate of solid column models, and (c) the general habit mixture and solid column models. The histograms show frequencies of occurrence on a log 10 scale, with red indicating the highest frequencies of occurrence.

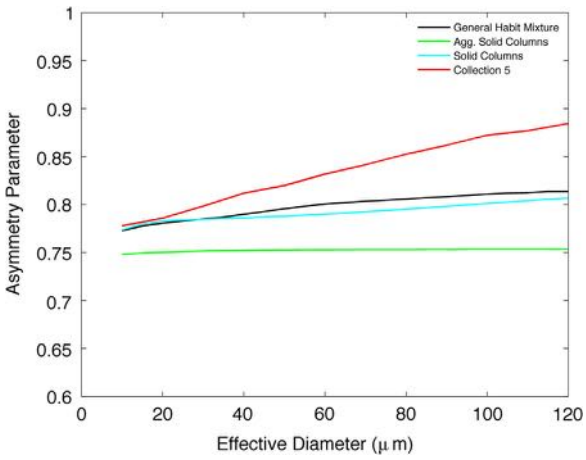


**Fig. 8.** The asymmetry parameter at 0.65 μm as a function of effective diameter for MODIS Collection 5 (red), the general habit mixture (black), solid columns (cyan), and the aggregate of solid columns (green).

models, and (c) the GHM and solid column model. For all three comparisons, the differences in optical thickness are very small, indicating that there is little sensitivity in the mid-IR (8–12 μm) to the choice of habit.

We now turn attention to solar-based optical thickness retrievals. Before showing results from the fast model, some insight can be gained by inspection of the asymmetry parameter at 0.65 μm for four different habit models. As shown in Fig. 8, the MODIS Collection 5 model has the highest asymmetry parameter values overall due to the assumption of smooth particles, and the values increase with particle size. The other three models assume the use of severely roughened particles, and the asymmetry parameter is lower for these models relative to the MODIS Collection 5 model. The model based on the aggregate of solid columns has the lowest values. Note that the value is fairly constant at 0.76 and invariant with particle size.

A higher value of the asymmetry parameter means that there is more energy in the forward scattered direction and less at side- and backscattering angles. This means

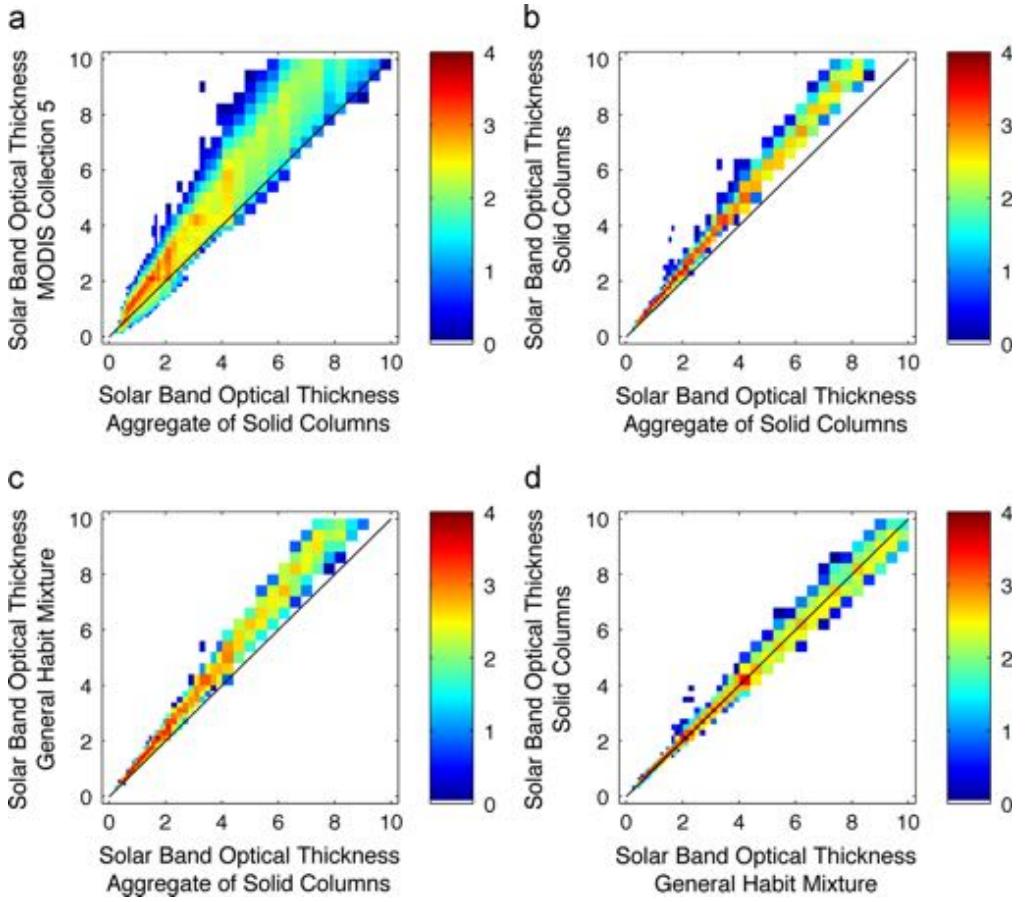


**Fig. 9.** Comparison of ice cloud optical thicknesses based on a fast model that infers optical thickness by minimizing the differences between model simulations and observations at 0.86 and 2.13 μm (MODIS bands 2 and 7, respectively). Results are shown that are based on different ice habit models for the MODIS granule shown in Fig. 3. Histograms are shown to compare results in (a) MODIS Collection 5 and the aggregate of solid columns, (b) the solid column and the aggregate of solid column models, (c) the general habit mixture and the aggregate of solid column models, and (d) the general habit mixture and solid column models. The histograms indicate frequencies of occurrence on a log 10 scale, with red indicating the highest frequencies of occurrence.

that more scattering will be required from the cloud to match a given reflectivity, and the increased scattering results in a higher inferred optical thickness. For a given set of measured reflectivities, the use of the MODIS Collection 5 model will result in higher inferred optical thicknesses than those inferred using the aggregate of solid column model.

Optical thickness results from the solar-channel fast model [41] are shown in Fig. 9 for the ice clouds in the image shown in Fig. 6. The panels in this figure show histograms of frequency of occurrence for retrievals based on the various ice habit models. To ease the interpretation of the results, a 1:1 line is included, and the visible optical thickness range of the results is limited to 10. Fig. 9 shows histograms to compare results in MODIS Collection 5 and the ASC (Fig. 9a), the SC and the ASC models (Fig. 9b), the GHM and ASC models (Fig. 9c), and the SC and GHM models (Fig. 9d). In Fig. 9a, note that the differences between the MODIS C5 and ASC models tend to increase with optical thickness, and there is a consistent bias in which the MODIS C5 optical thickness values are higher than those from the severely roughened aggregate of solid columns. Similar features are shown in Fig. 9b in the comparison of optical thickness values between the solid column model and the aggregate of solid column model. This is consistent with the asymmetry parameter being higher for the solid columns than for the aggregate of solid columns as shown in Fig. 5. Fig. 9c indicates that the optical thickness values for the GHM are higher than those inferred from use of the aggregate of solid columns. In fact, the GHM and solid column models have very similar values for the asymmetry parameter, so it is not surprising that the optical thickness values are also similar as shown in Fig. 9d.

The next step is to focus on the low optical thickness results to compare the IR- and solar-based optical thicknesses as shown in Fig. 10. A comparison of MODIS Collection 5 $\tau$ values between the solar and IR approaches is shown in Fig. 10a. As noted in earlier studies (e.g., [24]), the MODIS Collection 5 optical thicknesses are higher than those obtained by PARASOL. The $\tau$ values are limited in this figure compared to the solar-model results in Fig. 9 since the IR approach lacks sensitivity at higher values.

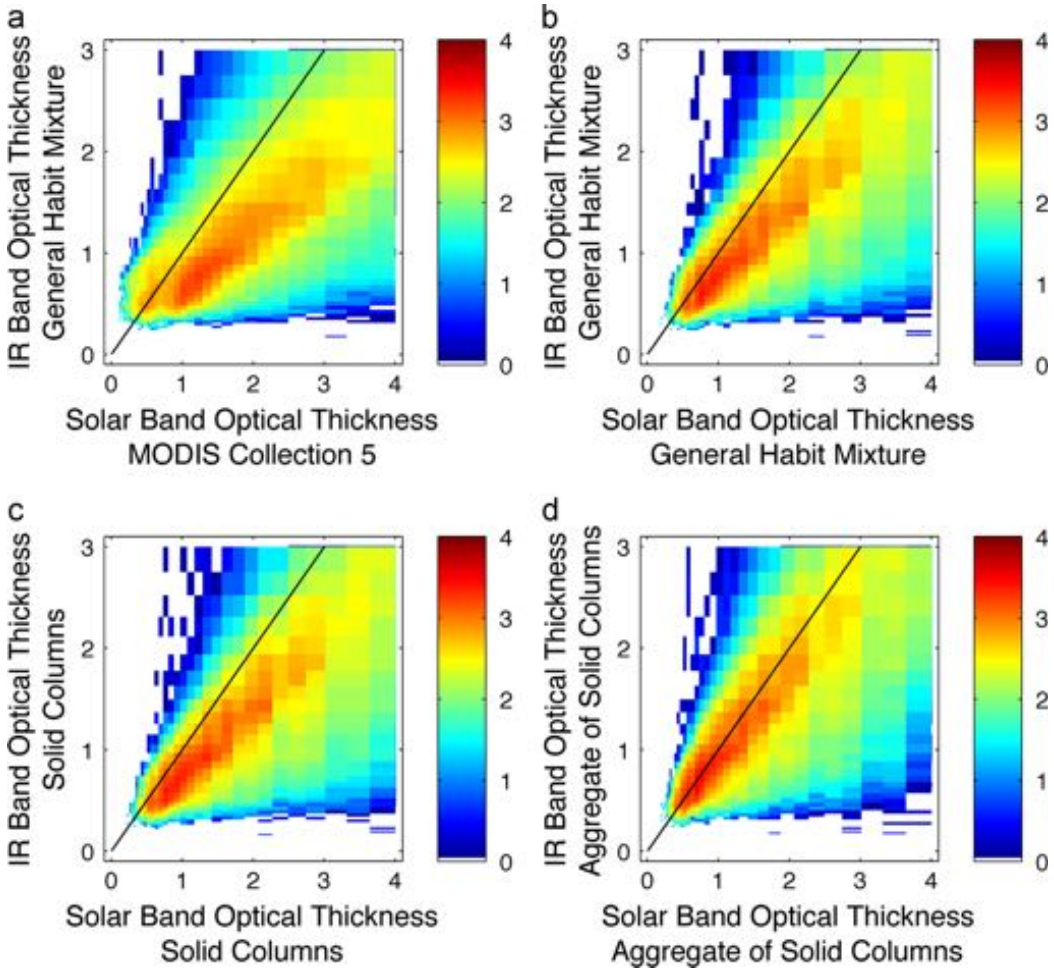


**Fig. 10.** Comparison of ice cloud optical thicknesses inferred separately from MODIS solar and IR bands. The results are based on different ice habit models for the MODIS granule shown in Fig. 3. Histograms are shown to compare results in (a) MODIS Collection 5 and the general habit mixture, (b) the general habit mixture, (c) the solid column model, and (d) the aggregate of solid column model. The histograms indicate frequencies of occurrence on a log 10 scale, with red indicating the highest frequencies of occurrence.

In Fig. 10a–c, the solar-based retrievals tend to be higher than the IR-based retrievals. However, given that the asymmetry parameter for the solid column, aggregate of solid column, and general habit mixture models are lower than that for Collection 5, the differences between the solar- and IR-based models decrease as expected. The aggregate of solid columns compares best with the IR-based retrievals, although the results suggest that the differences can increase as optical thickness increases.

## 4. Selected model results

The results in this section are provided separately for the shortwave region (0.2–5 μm) and longwave region (3.3–100 μm, or 100–3000 $cm^{-1}$).

Fig. 11 shows the model bulk single scattering properties obtained using the general habit mixture with severely roughened particles for the extinction efficiency, single scatter albedo, and asymmetry parameter as a function of wavelength and $D_{eff}$. The extinction efficiency is generally slightly above 2 when $D_{eff}=10$ μm and $\lambda < 2.6$ μm, but approximately 2 for higher values of $D_{eff}$. The scattering is conservative at non-absorbing wavelengths ($\tilde{\omega}=1$ for $\lambda < 1.4$ μm) but decreases at higher wavelengths when absorption increases within the ice particles. The asymmetry parameter tends to increase with $D_{eff}$. At 0.65 μm, the asymmetry parameter ranges from 0.77 to 0.81.

Fig. 12 shows the differences in these same properties between the GHM and SC models. The largest differences in extinction efficiency are noted at wavelengths between 2.5 and 3 μm. Relatively small differences are noted for the single scatter albedo, with differences no larger than 0.05 at any wavelength. The asymmetry parameter is shown to be slightly higher (by about 0.01) for the GHM models compared to the SC models at wavelengths below about 2.7 μm.

Similar results are shown in Fig. 13 for differences between the GHM and ASC models. It is apparent that

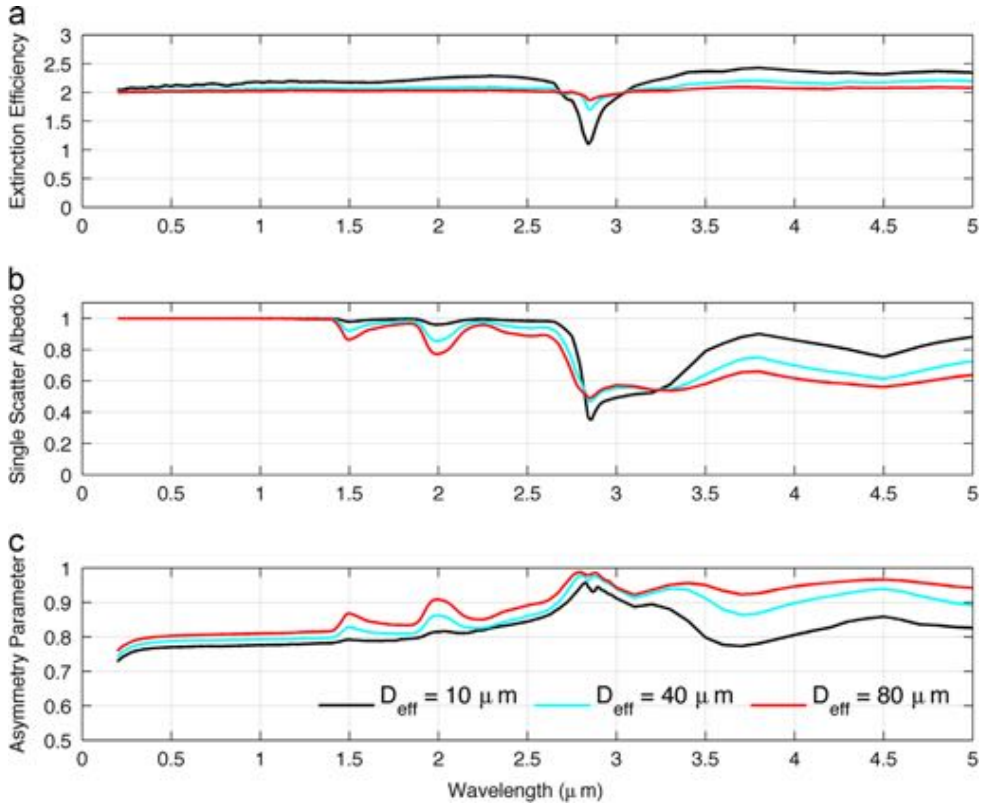


**Fig. 11.** Spectral results in the shortwave spectral region (0.2–5 μm) obtained using the general habit mixture with severe particle roughening for (a) extinction efficiency, (b) single scatter albedo, and (c) asymmetry parameter for effective diameters $D_{eff}$ of 10 μm, 40 μm, and 80 μm.

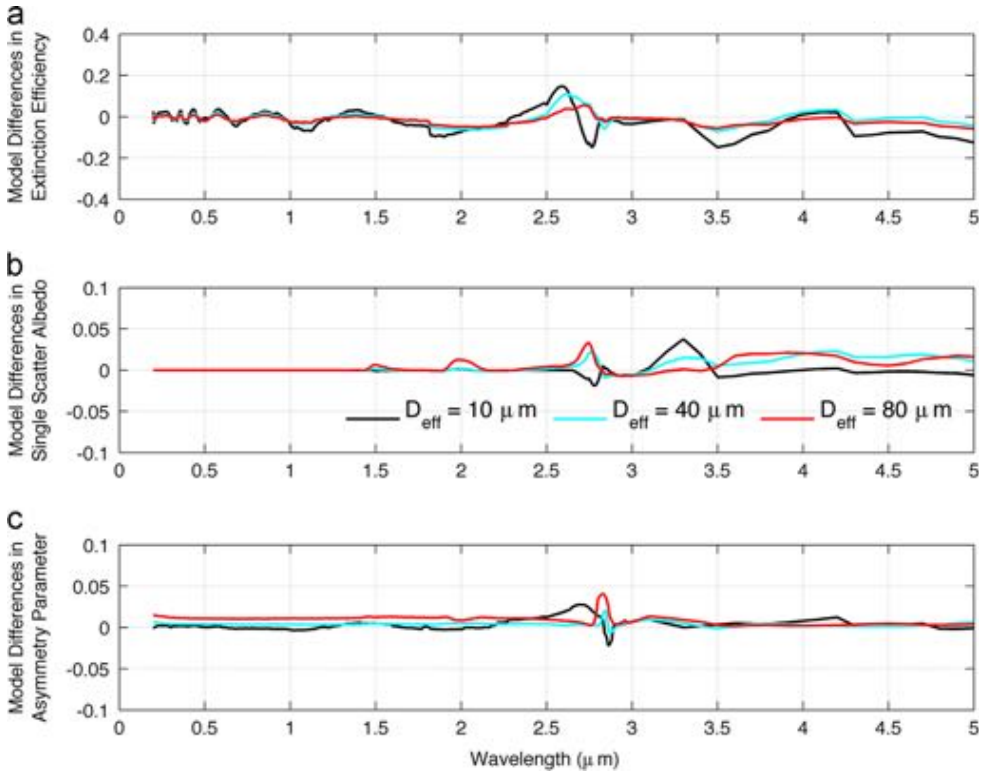


**Fig. 12.** Differences between the GHM and the solid column models in the shortwave spectral region (0.2–5 μm) for (a) extinction efficiency, (b) single scatter albedo, and (c) asymmetry parameter for effective diameters $D_{eff}$ of 10 μm, 40 μm, and 80 μm. Severely roughened particles are assumed for the models.

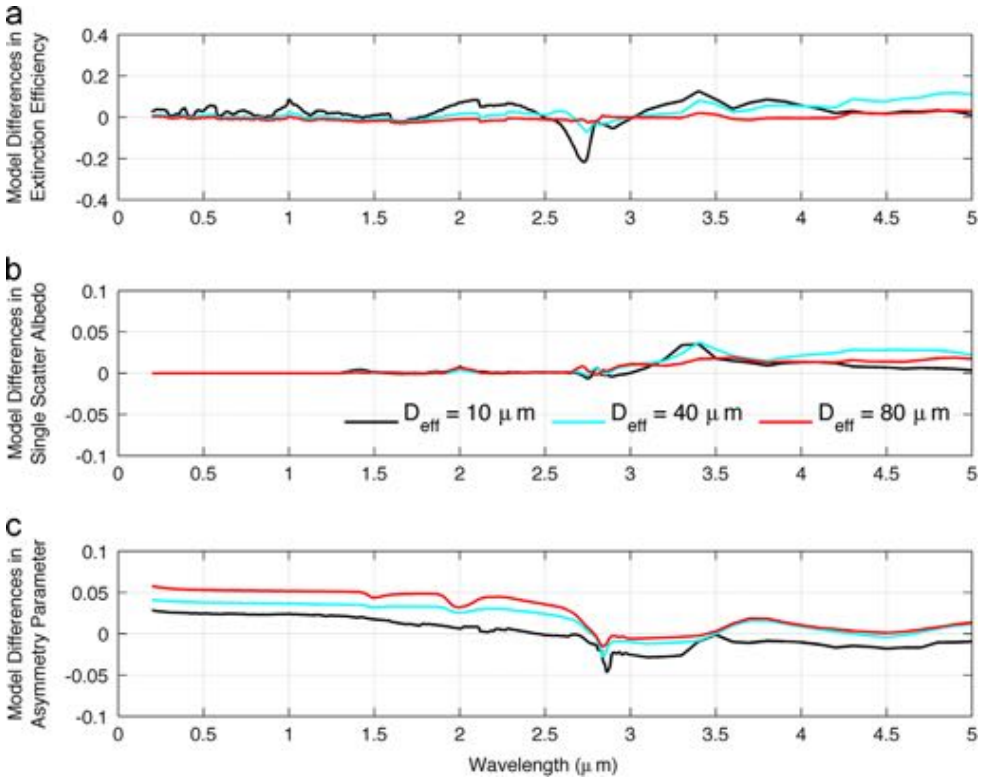


**Fig. 13.** Differences between the GHM and the aggregate of solid column models in the shortwave spectral region (0.2–5 μm) for (a) extinction efficiency, (b) single scatter albedo, and (c) asymmetry parameter for effective diameters $D_{eff}$ of 10 μm, 40 μm, and 80 μm. Severely roughened particles are assumed for the models.

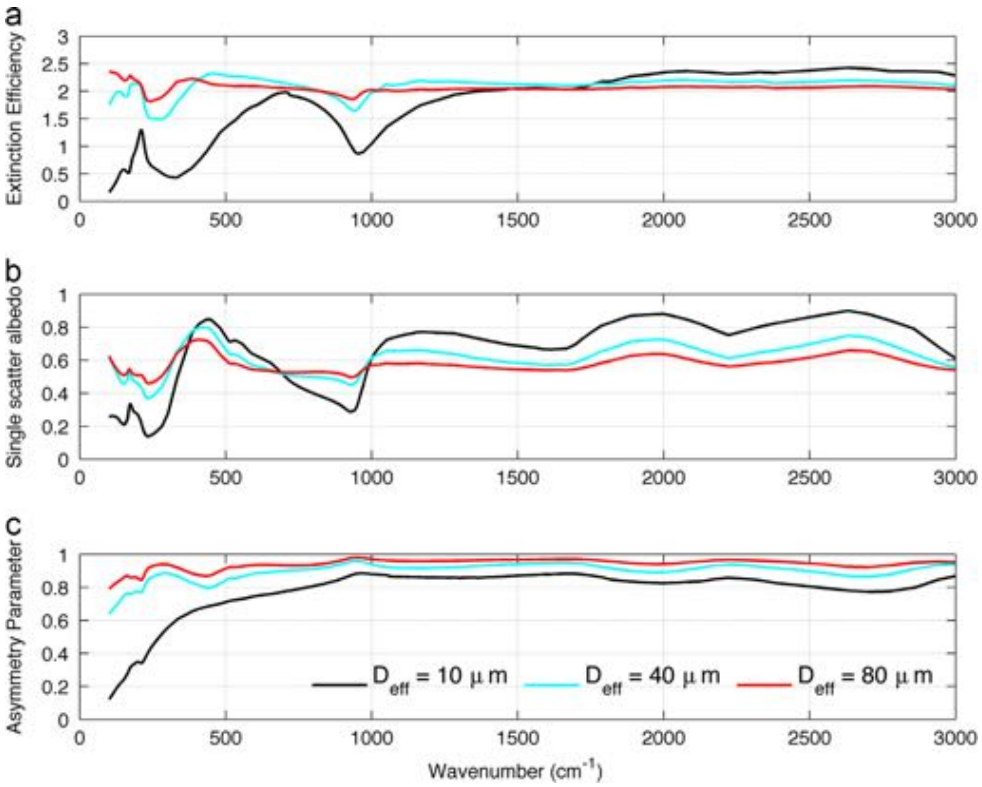


**Fig. 14.** Spectral results in the longwave spectral region (100–3000 $cm^{-1}$) obtained using the general habit mixture (GHM) with severe particle roughening for (a) extinction efficiency, (b) single scatter albedo, and (c) asymmetry parameter for effective diameters $D_{eff}$ of 10 μm, 40 μm, and 80 μm.

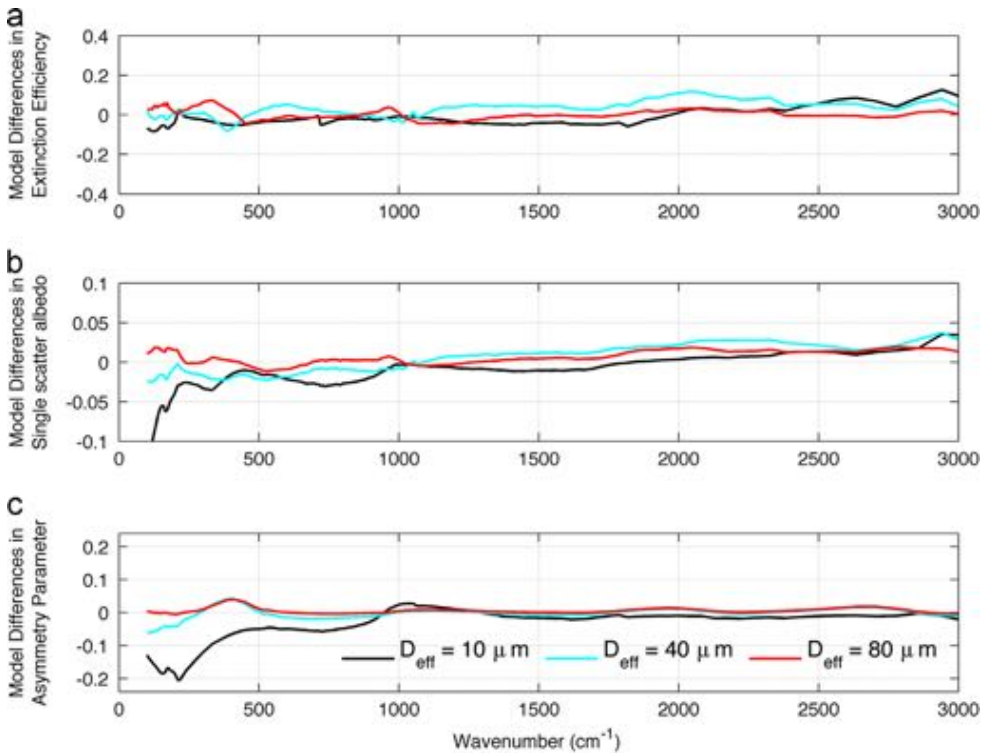


**Fig. 15.** Differences between the GHM and the aggregate of solid column models in the longwave spectral region (100–3000 $cm^{-1}$) for (a) extinction efficiency, (b) single scatter albedo, and (c) asymmetry parameter for effective diameters $D_{eff}$ of 10 μm, 40 μm, and 80 μm. Severely roughened particles are assumed for the models.

the asymmetry parameter is much larger for the GHM than for the aggregate of solid columns.

Results are shown in Fig. 14 at wavenumbers ($\nu$) from 100 to 3000 $cm^{-1}$ for the GHM, again assuming severe particle roughening. It has been shown earlier that roughening is not an issue in the mid-IR, nor is the choice of habit as important because of increased absorption within the ice particles. The increased absorption reduces the differences between the various ice habits that are found at solar wavelengths. The extinction efficiency (really the absorption efficiency at these long wavelengths) is close to 2 at wavenumbers between 1400 and 3000 $cm^{-1}$. With the various bulk properties, there is noted a dependence on $D_{eff}$ at the lower wavenumbers. The results here indicate that there is some potential in the Far-IR ($100 \leq \nu \leq 500\ cm^{-1}$) for inferring ice cloud properties for clouds containing smaller particles.

Fig. 15 shows that the differences are fairly small between the GHM and aggregate of solid column models. The only deviations of note are for the $D_{eff}$ models at 10 μm at Far-IR wavelengths. Similar results are not shown between the GHM and the solid column model because the differences are very small.

## 5. Summary and conclusions

Ice cloud bulk scattering models are derived for 445 discrete wavelengths between 0.2 μm and 100 μm. The methodology for deriving these optical models is reported in Baum et al. [1] and is based on microphysical data from 11 field campaigns using a variety of in situ probes, and incorporates a correction to mitigate the impact of ice particles that shatter at the probe inlets. The models are also based on a new library of ice habit single scattering properties developed for plates, droxtals, hollow and solid columns, hollow and solid bullet rosettes, an aggregate of solid columns, and a small/large aggregate of plates [33]. Three sets of models are developed that assume the use of solid columns only, the aggregate of solid columns only, and a general habit mixture that involves all nine habits.

The consistency of the resulting models is explored through comparison with in situ measurements and sensors in the NASA A-Train constellation. The microphysical properties of IWC and $D_{mm}$ for each of the assumed habit distributions is compared to those obtained from in situ measurements. The solid columns compare most closely with the in situ microphysical data, while those based on the general habit mixture are generally within a factor of 2 or better. The aggregate of solid column model underestimates IWC especially at low values, and overestimates $D_{mm}$ at high values.

Another test of model consistency is to compare the polarization properties based on the models to those measured from PARASOL. The habit mixture provides close agreement with measured polarized reflectivities for all effective diameters $D_{eff}$ and for four days of data from different seasons. However, neither the solid column nor the aggregate of solid column models compare as closely at any $D_{eff}$.

A final consistency test is to investigate the agreement in optical thickness obtained at solar and IR wavelengths.

The IR models are not sensitive to habit because of the stronger absorption within the particles. The solar models are much more sensitive to habit. A test is performed for a MODIS scene over the Bay of Bengal. The aggregate of solid columns provides the closest agreement; this is most likely due to this habit having the lowest asymmetry parameter of all the habits that is nearly constant with $D_{eff}$ at about 0.76.

Finally, spectral results are presented for the shortwave and longwave models. The various parameters are now smooth across the spectrum, and do not suffer from spectral gaps or discontinuities in properties that were caused, in earlier models, in transitioning from one scattering model to another across the range of particle sizes and wavelengths.

## Acknowledgments

Bryan Baum, Andy Heymsfield, and Ping Yang gratefully acknowledge the support provided through NASA Grants NNX11AR06G and NNX11AF40G. The authors thank Dr. Hal Maring for his encouragement and support over the years. We also gratefully acknowledge the anonymous reviewers for their time and effort in helping us improve this manuscript.

## Appendix A

### *Bulk microphysical properties*

For a given particle size distribution (PSD), the total projected area and total volume of ice per unit volume of air are given by

$$A_{tot} = \sum_{h=1}^{M} \left[ \int_{D_{min}}^{D_{max}} A_h(D) f_h(D) n(D)\, dD \right], \tag{A.1}$$

and

$$V_{tot} = \sum_{h=1}^{M} \left[ \int_{D_{min}}^{D_{max}} V_h(D) f_h(D) n(D)\, dD \right], \tag{A.2}$$

respectively, where $D_{min}$ and $D_{max}$ describe the minimum and maximum particle sizes in the distribution, $f_h(D)$ is the ice particle habit fraction of habit $h$ for size $D$, $n(D)$ is the number distribution for size $D$, and $A_h(D)$ and $V_h(D)$ are the projected area and volume of a specific particle of habit $h$ for size $D$, respectively. The habit fraction is defined so that for each size bin,

$$\sum_{h=1}^{M} f_h(D) = 1. \tag{A.3}$$

The ice water content (IWC) for a given PSD is

$$IWC = \rho_{ice} \sum_{h=1}^{M} \left[ \int_{D_{min}}^{D_{max}} V_h(D) f_h(D) n(D)\, dD \right], \tag{A.4}$$

where $\rho_{ice} = 0.917$ g cm$^{-3}$.

The effective diameter $D_{eff}$ [43] is defined as

$$D_{eff} = \frac{3}{2} \frac{\sum_{h=1}^{M} \left[ \int_{D_{min}}^{D_{max}} V_h(D) f_h(D) n(D)\, dD \right]}{\sum_{h=1}^{M} \left[ \int_{D_{min}}^{D_{max}} A_h(D) f_h(D) n(D)\, dD \right]} = \frac{3}{2} \frac{V_{tot}}{A_{tot}}. \tag{A.5}$$

### *Spectral bulk scattering properties*

In this section, the single-scattering properties are derived at a specific wavelength following [1]. Examples are provided here for selected parameters. The mean extinction cross section is given by

$$\overline{\sigma}_{ext}(\lambda) = \frac{\int_{D_{min}}^{D_{max}} [\sum_{h=1}^{M} \sigma_{ext,h}(D,\lambda) f_h(D)] n(D)\, dD}{\int_{D_{min}}^{D_{max}} [\sum_{h=1}^{M} f_h(D)] n(D)\, dD}. \tag{A.6}$$

The scattering cross section is calculated similarly. The single-scattering albedo $\overline{\omega}$ is determined by the ratio of the mean scattering and extinction cross sections:

$$\overline{\omega}(\lambda) = \frac{\overline{\sigma}_{sca}(\lambda)}{\overline{\sigma}_{ext}(\lambda).} \tag{A.7}$$

The scattering phase function $\overline{P}(\Theta)$ is given by

$$\overline{P}(\Theta,\lambda) = \frac{\int_{D_{min}}^{D_{max}} [\sum_{h=1}^{M} P_h(\Theta,D,\lambda) \sigma_{sca,h}(D,\lambda) f_h(D)] n(D)\, dD}{\int_{D_{min}}^{D_{max}} [\sum_{h=1}^{M} \sigma_{sca,h}(D,\lambda) f_h(D)] n(D)\, dD}, \tag{A.8}$$

where $\Theta$ is the scattering angle.

The asymmetry parameter ($\overline{g}$) is given by

$$\overline{g}(\lambda) = \frac{\int_{D_{min}}^{D_{max}} [\sum_{h=1}^{M} g_h(D,\lambda) \sigma_{sca,h}(D,\lambda) f_h(D)] n(D)\, dD}{\int_{D_{min}}^{D_{max}} [\sum_{h=1}^{M} \sigma_{sca,h}(D,\lambda) f_h(D)] n(D)\, dD}. \tag{A.9}$$

### *Narrowband bulk scattering properties*

To build narrowband bulk single-scattering properties appropriate for an imager such as MODIS, the spectral single-scattering properties need to be integrated over a spectral response function. An example is provided for calculating the asymmetry parameter; the other parameters are integrated similarly.

$$\langle \overline{g} \rangle = \frac{\int_{\lambda_{min}}^{\lambda_{max}} \overline{g}(\lambda) F_s(\lambda) S(\lambda)\, d\lambda}{\int_{\lambda_{min}}^{\lambda_{max}} F_s(\lambda) S(\lambda)\, d\lambda}, \tag{A.10}$$

where $S(\lambda)$ is the solar irradiance at solar wavelengths (but this term switches to the Planck function in the IR, assuming a cloud temperature of 233K) and $F_s(\lambda)$ is the spectral response function. In this study, the Thuillier solar spectrum is used for integrating over the spectral response functions [44].

## References

[1] Baum BA, Yang P, Heymsfield AJ, Schmitt CG, Xie Y, Bansemer A, et al. Improvements to shortwave bulk scattering and absorption models for the remote sensing of ice clouds. J Appl Meteorol Clim 2011;50:1037–56.

[2] Mitchell DL. Effective diameter in radiation transfer: general definition, applications, and limitations. J Atmos Sci 2002;59:2330–46.

[3] Wyser K, Yang P. Average ice crystal size and bulk short-wave single-scattering properties of cirrus clouds. Atmos Res 1998;49:315–35.
[4] Wyser K. The effective radius in ice clouds. J Clim 1998;11:1793–802.
[5] Nakajima T, King MD. Determination of the optical thickness and effective particle radius of clouds from reflected solar radiation measurements. 1. Theory. J Atmos Sci 1990;47:1878–93.
[6] Platnick S. Vertical photon transport in cloud remote sensing problems. J Geophys Res 2000;105(D18):22919–35.
[7] Platnick S, King MD, Ackerman SA, Menzel WP, Baum BA, Riedi JC, et al. The MODIS cloud products: algorithms and examples from Terra. IEEE Trans Geosci Remote Sens 2003;41:459–73.
[8] Walther A, Heidinger AK. Implementation of the daytime cloud optical and microphysical properties algorithm (DCOMP) in PATMOS-x. J Appl Meteorol Climatol 2012;51:1371–90.
[9] Minnis P, Sun-Mack S, Young DF, Heck PW, Garber DP, et al. CERES edition-2 cloud property retrievals using TRMM VIRS and Terra and Aqua MODIS data – Part I: algorithms. IEEE Trans Geosci Remote Sens 2011;49:4374–400.
[10] Iwabuchi H, Yamada S, Katagiri S, Yang P, Okamoto H. Radiative and microphysical properties of cirrus clouds inferred from the infrared measurements made by the Moderate Resolution Imaging Spectro-radiometer (MODIS). Part I: retrieval method. J Appl Meteorol Climatol 2014. http://dx.doi.org/10.1175/JAMC-D-13-0215.1.
[11] Garnier A, Pelon J, Dubuisson P, Faivre M, Chomette O, Pascal N, et al. Retrieval of cloud properties using CALIPSO Imaging Infrared Radiometer. Part I: effective emissivity and optical depth. J Appl Meteorol Climatol 2012;51:1407–25.
[12] Ou SC, Kahn BH, Liou KN, Takano Y, Schreier MM, Yue Q. Retrieval of cirrus cloud properties from the Atmospheric Infrared Sounder: the k-coefficient approach combined with SARTA plus delta-four stream approximation. IEEE Trans Geosci Remote Sens 2013;51:1010–24.
[13] Yue Q, Liou KN. Cirrus cloud optical and microphysical properties determined from AIRS infrared spectra. Geophys Res Lett 2009;36: L05810.
[14] Buriez JC, Vanbauce C, Parol F, Goloub P, Herman M, Bonnel B, et al. Cloud detection and derivation of cloud properties from POLDER. Int J Remote Sens 1997;18:2785–813.
[15] Baran AJ, Labonotte LC. On the reflection and polarisation properties of ice cloud. J Quant Spectrosc Radiat Transf 2006;100:41–54.
[16] Chepfer H, Goloub P, Spinhirne P, Flamant PH, Lavorato M, Sauvage L, et al. Cirrus cloud properties derived from POLDER-1/ADEOS polarized radiances: first validation using a ground-based lidar network. J Appl Meteorol 2000;39:154–68.
[17] C-Labonnote L, Brogniez G, Doutriaux-Boucher M, Buriez JC, Gayet JF, Chepfer H. Modeling of light scattering in cirrus clouds with inhomogeneous hexagonal monocrystals. Comparison with In-situ and ADEOS-POLDER measurements. Geophys Res Lett 2000;27: 113–6.
[18] Wang C, Yang P, Platnick S, Heidinger AK, Baum BA, Greenwald T, et al. Retrieval of ice cloud properties from AIRS and MODIS observations based on a fast high-spectral-resolution radiative transfer model. J Appl Meteorol Climatol 2013;52:710–26.
[19] Cooper S, L'Ecuyer T, Gabriel PK, Baran A, Stephens G. Objective assessment of the information content of visible and infrared radiance measurements for cloud microphysical property retrievals over the global oceans. Part 2: ice clouds. J Appl Meteorol 2006;45: 42–62.
[20] Knap WH, C-Labonnote L, Brogniez G, Stammes P. Modeling total and polarized reflectances of ice clouds: evaluation by means of POLDER and ATSR-2 measurements. Appl Opt 2005;44:4060–73.
[21] Baum BA, Kratz DP, Yang P, Ou SC, Hu Y, Soulen PF, et al. Remote sensing of cloud properties using MODIS Airborne Simulator imagery during SUCCESS. I. Data and models. J Geophys Res 2000;105: 11767–80.
[22] Winker DM, Vaughan MA, Omar A, Hu YX, Powell KA, Liu ZY, et al. Overview of the CALIPSO mission and CALIOP data processing algorithms. J Atmos Ocean Technol 2009;26:2310–23.
[23] Vaughan MA, Powell KA, Kuehn RE, Young SA, Winker DM, Hostetler CA, et al. Fully automated detection of cloud and aerosol layers in the CALIPSO lidar measurements. J Atmos Ocean Technol 2009;26: 2034–50.
[24] Zhang Z, Yang P, Kattawar GW, Riedi J, Labonnote LC, Baum BA, et al. Influence of ice particle model on satellite ice cloud retrieval: lessons learned from MODIS and POLDER cloud product comparison. Atmos Chem Phys 2009;9:7115–29.
[25] Baum BA, Yang P, Hu YX, Feng Q. The impact of ice particle roughness on the scattering phase matrix. J Quant Spectrosc Radiat Transf 2010;111:2534–49. http://dx.doi.org/10.1016/j.jqsrt.2010.07.008.
[26] Cole B, Yang P, Baum BA, Riedi J, Labonnote CL, Thieuleux F, et al. Comparison of PARASOL observations with polarized reflectances simulated using different ice habit mixtures. J Appl Meteorol Clim 2013;52:186–96.
[27] Heymsfield AJ, Schmitt CG, Bansemer A. Ice cloud particle size distributions and pressure-dependent terminal velocities from in situ observations at temperatures from 0 to −86 C. J Atmos Sci 2013;70:4123–54. http://dx.doi.org/10.1175/JAS-D-1209124.1.
[28] Schmitt CG, Heymsfield AJ. The size distribution and mass-weighted terminal velocity of low-latitude cirrus crystal populations. J Atmos Sci 2009;66:2013–28.
[29] Korolev AV, Isaac GA. Shattering during sampling by OAPs and HVPS. Part 1: snow particles. J Atmos Ocean Technol 2005;22:528–42.
[30] Korolev AV, Emery EF, Strapp JW, Cober SG, Isaac GA, Wasey M, et al. Small ice particles in tropospheric clouds: fact or artifact? Airborne icing instrumentation evaluation experiment Bull Am Meteorol Soc 2011;92:967–73.
[31] Field PR, Heymsfield AJ, Bansemer A. Shattering and particle inter-arrival times measured by optical array probes in clouds. J Atmos Ocean Technol 2006;23:1357–71.
[32] deReus MS, Borrmann S, Bansemer A, Heymsfield AJ, Weigel R, Schiller C, et al. Evidence for ice particles in the tropical stratosphere from in–situ measurements. Atmos Chem Phys 2009;9: 6775–92. http://dx.doi.org/10.5194/acp-9-6775-2009.
[33] Yang P, Bi L, Baum BA, Liou KN, Kattawar GW, Mishchenko M. Spectrally consistent scattering, absorption, and polarization properties of atmospheric ice crystals at wavelengths from 0.2 μm to 100 μm. J Atmos Sci 2013;70:330–47.
[34] Ulanowski Z, Hesse E, Kaye PH, Baran AJ. Light scattering by complex ice-analogue crystals. J Quant Spectrosc Radiat Transf 2006;100: 382–92.
[35] Ulanowski Z, Hirst E, Kaye PH, Greenaway R. Retrieving the size of particles with rough and complex surfaces from two-dimensional scattering patterns. J Quant Spectrosc Radiat Transf 2012;113: 2457–64.
[36] Yang P, Kattawar GW, Hong G, Minnis P, Hu YX. Uncertainties associated with the surface texture of ice particles in satellite-based retrieval of cirrus clouds: Part I. Single-scattering properties of ice crystals with surface roughness. IEEE Trans Geosci Remote Sens 2008;46:1940–7.
[37] Bi L, Yang P, Kattawar GW, Baum BA, Hu YX, Lu JQ. Simulation of the color ratio associated with the backscattering of radiation by ice crystals at 0.532 and 1.064-μm wavelengths. J Geophys Res 2009;114:D00H08. http://dx.doi.org/10.1029/2009JD011759.
[38] Takano Y, Liou KN. Solar radiative transfer in cirrus clouds. Part I. Single-scattering and optical properties of hexagonal ice crystals. J Atmos Sci 1989;46:3–19.
[39] Warren SG, Brandt RE. Optical constants of ice from the ultraviolet to the microwave: a revised compilation. J Geophys Res 2008;113: D14220. http://dx.doi.org/10.1029/2007JD009744.
[40] Cole B, Yang P, Baum BA, Riedi J, Labononote CL. Ice particle habit and roughness derived from PARASOL polarization measurements. Atmos Chem Phys Disc 2013;13:29483–519. http://dx.doi.org/10.5194/acpd-13-29483-2013.
[41] Wang C, Yang P, Nasiri SL, Platnick S, Baum BA, Liu X, et al. A fast radiative transfer model in the visible and shortwave infrared region. J Quant Spectrosc Radiat Transf 2013;116:122–31. http://dx.doi.org/10.1016/j.jqsrt.2012.10.012.
[42] Wang C, Yang P, Baum BA, Platnick S, Heidinger AK, Hu YX, et al. Retrieval of ice cloud optical thickness and effective particle size using a fast infrared radiative transfer model. J Appl Meteorol Clim 2011;50:2283–97. http://dx.doi.org/10.1175/JAMC-D-11-067.1.
[43] Foot JS. Some observations of the optical properties of clouds: II cirrus. Quart J R Meteorol Soc 1988;114:145–64.
[44] Thuillier G, Hersé M, Simon PC, Labs D, Mandel H, Gillotay D, et al. The solar spectral irradiance from 200 to 2400 nm as measured by the SOLSPEC spectrometer from the ATLAS 1-2-3 and EURECA missions. Sol Phys 2003;214:1–22.